www.springer.com/41230
https://doi.org/10.1007/s41230-025-5127-5

Tuning needle-like precipitation for enhanced strength-ductility synergy in a non-equiatomic FeNiCoCuTi high-entropy alloy

Li-ran Huang[1, 2], **Zhi-ming Li**[3], **Wei-ping Chen**[1, 2], and ***Zhi-qiang Fu**[1, 2]

1. Guangdong Key Laboratory for Advanced Metallic Materials Processing, South China University of Technology, Guangzhou 510640, China

2. National Engineering Research Center of Near-net-shape Forming for Metallic Materials, South China University of Technology, Guangzhou 510640, China

3. School of Materials Science and Engineering, Central South University, Changsha 410083, China

Abstract: Precipitation strengthening is an effective strengthening strategy widely utilized in high-entropy alloys (HEAs) with a single-phased face-centered cubic (fcc) structure. In recent research works, reinforcing phase adopted are mostly focused on equiaxed or nearly equiaxed structures (e.g., spherical, cubic, and rod-like), while relatively rare studies on the strengthening effects of needle-like precipitates with large aspect ratios. The η-$D0_{24}$ phase, like the $L1_2$ strengthening phase most commonly used in fcc-structured HEAs, features an ordered Ni_3Ti-type structure and also exhibits a comparable strengthening effect. However, since the η phase often co-precipitates with other precipitates in alloy system, the strengthening effect of the sole η-$D0_{24}$ phase in fcc-structured alloys remains to be further explored. In this study, microstructural evolution, phase transformation, and mechanical behaviors of a non-equiatomic $Fe_{27}Ni_{27}Co_{26}Cu_{10}Ti_{10}$ HEA were systematically investigated. Results show that following high-temperature heat treatment, the microstructure of the studied HEA transforms from a combination of the fcc, $L1_2$, Cu-rich, and η phases in the as-cast state to a fcc+η structure in the heat-treated state. Meanwhile, the mechanical properties of the heat-treated HEA are significantly improved, with a total elongation increasing from approximately 0.9% to 7.5%. The enhanced ductility of the heat-treated alloy can be attributed to the strong hindering effect of numerous needle-like η phase at the grain boundaries, which restricts crack propagation and dislocation movement. This study develops a novel η-strengthened FeNiCoCuTi HEA, expanding the selection of available reinforcing phases in fcc-structured alloys and providing valuable insights into the phase transformation and strengthening effect of the η-$D0_{24}$ phase.

Keywords: high-entropy alloys; η-$D0_{24}$ phase; microstructural evolution; phase transformation; mechanical behavior

CLC numbers: TG143 **Document code:** A **Article ID:** 1672-6421(2026)03-303-12

1 Introduction

High-entropy alloys (HEAs) or multi-principal-element alloys (MPEAs) with various excellent properties and unique characteristics have become one of the hot research topics in metal materials[1, 2]. Face-centered cubic (fcc) structured HEAs are particularly notable for their high ductility, outstanding impact toughness, attractive strain hardening capacity, and good corrosion resistance[3-5]. However, due to the inherent feature of the crystal structure, the yield strength of fcc-structured HEAs, especially polycrystalline HEAs, is usually unsatisfactory, making it challenging to meet industrial demands[6, 7]. Plentiful studies have focused on improving the moderate strength of the fcc-structured HEAs, with commonly used strengthening strategies including solid solution strengthening, grain refinement strengthening, precipitation strengthening, and heterogeneous strengthening[8-11]. Precipitation

---

***Zhi-qiang Fu**

Male, born in 1986, Ph. D., Professor. His research interests mainly focus on alloy design, manufacturing and processing of critical metallic materials used in extreme environments.

E-mail: zhiqiangfu2019@scut.edu.cn

Received: 2025-06-09; Revised: 2025-07-31; Accepted: 2025-08-25

strengthening stands out among multiple strengthening mechanisms by its remarkable strengthening effect and adjustable performance, achievable through simplified alloying and heat treatment processes[12, 13].

Numerous reinforcing phases can be introduced into single-phase fcc matrix, including ordered fcc-structured $L1_2$, disordered body-centered cubic (bcc), ordered bcc-structured B2, topological closed packed (tcp) structured σ, μ, and Laves, ordered hexagonal close-packed (hcp) structured η-$D0_{24}$, and so on[14-18]. Among them, ordered $L1_2$ phase is the most widely used strengthening phase in fcc-structured HEAs, which can significantly improve strength without a substantial loss in ductility[19, 20]. For instance, Yang et al.[14] reported a $L1_2$-strengthened Ni-30Co-13Fe-15Cr-6Al-6Ti-0.1B HEA by duplex-aging treatment, achieving a remarkable improvement of strength and ductility. Conversely, the ordered η-$D0_{24}$ phase, which shares the same Ni_3Ti-type structure as the $L1_2$ phase, is generally considered deleterious in fcc-structured alloys[21]. In fact, the η-$D0_{24}$ phase with proper distribution and volume fraction can also enhance strength under the premise of limited ductility reduction[22]. The morphologies of $L1_2$ or B2 phases typically exhibit equiaxed or near-equiaxed characteristics (e.g., spherical, cubic, and rod-like), whereas needle-like η phase, distinctively, has a significantly larger aspect ratio with pronounced anisotropy. This morphological difference results in needle-like η phase having a stronger ability to impede dislocation movement than $L1_2$ or B2 phases, leading to a superior strengthening effect. Since the η-$D0_{24}$ phase typically occurs in conjunction with other precipitates, its individual contribution to strengthening is rarely isolated or studied[23].

Introducing the η-$D0_{24}$ phase selectively into fcc HEAs without concurrent formation of other precipitates remains a significant challenge. Based on our previous findings, the $L1_2$ and η-$D0_{24}$ phases can undergo mutual transformation under specific thermal or compositional conditions[24]. Therefore, the objective of this work is to achieve a microstructure comprising fcc and η phases via the combination of tailoring composition and simplified heat treatment process. Titanium (Ti) is a crucial element to promote the formation of η-$D0_{24}$ phase[25], so a high concentration of Ti (10at.%) was involved in the alloy. In the present work, a non-equiatomic $Fe_{27}Ni_{27}Co_{26}Cu_{10}Ti_{10}$ (at.%) HEA was proposed. The designed HEA was arc melted to obtain the as-cast sample, which was subsequently held at 1,000 °C for 4 h to obtain the heat-treated sample. The microstructural evolution and phase transformation during the heat treatment progress were discussed in detail, and the impact of the sole η-$D0_{24}$ phase on the mechanical properties of the FeNiCo fcc-structured HEA was systematically investigated.

2 Material and methods

2.1 Materials preparation

The investigated alloy with a nominal composition of $Fe_{27}Ni_{27}Co_{26}Cu_{10}Ti_{10}$ (at.%) was fabricated via magnetic levitation melting. Pure bulk metals of Fe, Ni, Co, Cu, and Ti with high purity (≥99.5wt.%) were used as raw materials. The ingots were remelted at least five times to avoid element segregation, and the entire melting process was performed under a high purity argon atmosphere. The as-cast samples were homogenized at 1,000 °C for 4 h with flowing argon gas to assuage elemental segregation during solidification and followed by water quenching, then, the heat-treated samples were obtained.

2.2 Microstructure characterization

The phase constitution of as-cast and heat-treated samples was identified by X-ray diffractometer (XRD, X'Pert Pro PANalytical) using Cu-Kα radiation with a scanning range of 20°–100°. The electron backscattered diffraction (EBSD, JEOL 7100F equipped with a field emission gun) measurement with an accelerating voltage of 15 kV was conducted to observe the average grain size and grain orientation. The microstructure of the studied HEA was characterized using scanning electron microscopy (SEM, FE-SEM, JEOL, JSM-7800F) equipped with a backscattering electron (BSE) detector. To further investigate the nanoscale microstructural features, crystallography, and local chemical composition, high-resolution transmission electron microscopy (TEM, FEI Talos F200X) was employed, equipped with selected area electron diffraction (SAED) and energy dispersive spectroscopy (EDS). EDS measurement was conducted on the scanning transmission electron microscopy (STEM) mode. To accurately investigate the chemical distribution at the sub-nanometer scale, atom probe tomography (APT, LEAP^{TM} 3000X HR) was employed with a acquisition temperature of 70 K, a pulse frequency of 200 kHz, and a pulse fraction of 15%. The target detection rate was set to 0.4%, corresponding to an average of 4 detection events per 1,000 pulses. The 3D atomic map reconstruction, visualization, and all data analysis were performed using the IVAS® 3.6.14 software. The needle-shaped APT specimen was fabricated by dual beam focused-ion-beam (FIB, Helios Nanolab600/600i).

2.3 Mechanical property testing

Mechanical properties of the as-cast and heat-treated samples were investigated by tensile testing at room temperature. The dog-bone shaped tensile specimens with gauge dimensions of 10 mm×2.5 mm×1.0 mm (length×width×thickness) were fabricated by electrical discharge machining. The tensile tests were carried out on a Zwick/Roell Z020 universal testing machine with an engineering rate of 1×10^{-3} s^{-1} at room temperature, and each sample was repeated at least three times to ensure the reliability of the data. After tensile testing, the fracture morphology of the tensile specimens was characterized by SEM on the secondary electron mode.

3 Results and discussion

3.1 Microstructural evolution

As shown in Fig. 1, XRD patterns of both the as-cast and heat-treated $Fe_{27}Ni_{27}Co_{26}Cu_{10}Ti_{10}$ HEA exhibit two types of diffraction peaks, corresponding to the fcc structure and η structure, respectively. The fcc phase exhibits a greater number of diffraction peaks and higher peak intensities compared to the η phase, indicating that the fcc structure is the predominant phase in both the as-cast and heat-treated samples. The EBSD phase map and inverse pole figure (IPF) map in Fig. 2 reveal that the grains in as-cast $Fe_{27}Ni_{27}Co_{26}Cu_{10}Ti_{10}$ HEA are equiaxed and exhibit a single-phase fcc structure. The lack of observable η-phase regions in the phase map [Fig. 2(a)] is likely due to its low volume fraction or sub-resolution size, which falls below the detection limit of EBSD. Additionally, grain boundaries of the as-cast sample are predominantly composed of high-angle grain boundaries (HAGBs, higher than 15°) with a minor presence of low-angle grain boundaries (LAGBs, 2°–15°). The average grain size of the as-cast sample is obtained to be approximately 37.3 μm.

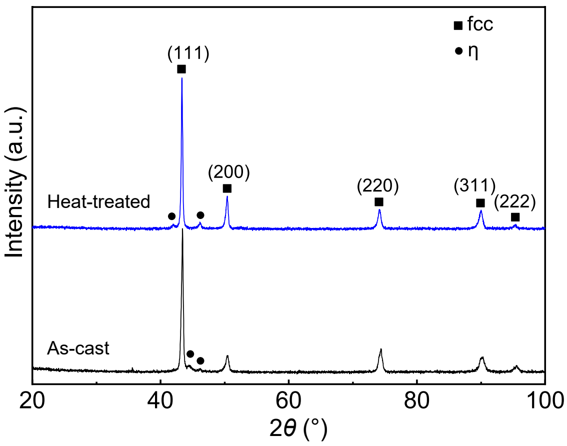

Fig. 1: XRD patterns of as-cast and heat-treated $Fe_{27}Ni_{27}Co_{26}Cu_{10}Ti_{10}$ HEA samples

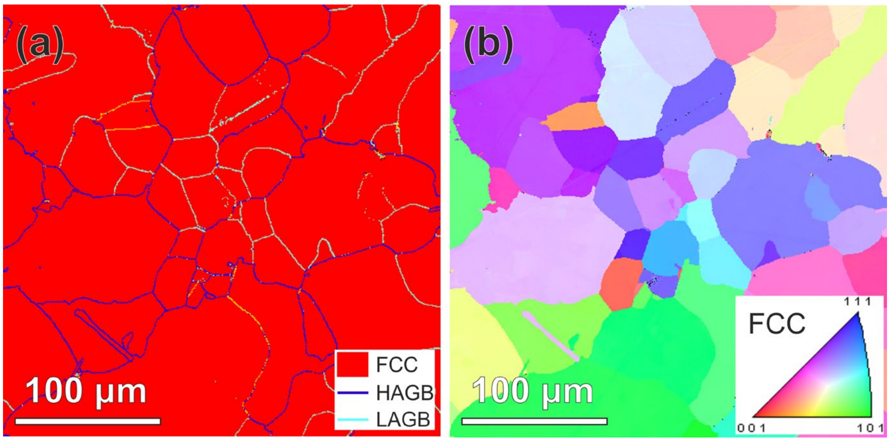

Fig. 2: EBSD phase map (a) and inverse pole figure map (b) of as-cast $Fe_{27}Ni_{27}Co_{26}Cu_{10}Ti_{10}$ HEA

The microstructure of the as-cast $Fe_{27}Ni_{27}Co_{26}Cu_{10}Ti_{10}$ HEA is presented in Fig. 3. In the low- and high-magnification SEM images [Figs. 3(a–b)], the equiaxed grains (grey region) and some uncertain phases (white region) near the grain boundaries can be visibly observed. When the region near the grain boundaries is magnified, a large amount of near-spherical precipitates can be observed, as shown in Figs. 3(b–c). Other magnified images of the grain boundary [Figs. 3(d–e)] display some needle-like phase generated at the grain boundaries. The crystal structure of these two phases will be identified by TEM and APT analysis in the later section. In contrast, the high-magnification SEM image of the transgranular region [Fig. 3(f)] manifests the absence of precipitates inside the grains. Additionally, the EDS results of the Points 1, 2, and 3 in Fig. 3 are summarized in Table 1. Point 1, corresponding to the grain interior of the as-cast sample, exhibits a composition of 30.80at.% Fe, 26.16at.% Ni, 26.42at.% Co, 8.87at.% Cu, and 7.75at.% Ti, which is in close agreement with the nominal alloy composition. Meanwhile, the EDS results of Points 2 and 3 demonstrate a preferential concentration of Ni-Ti in the needle-like phase and a slight enrichment tendency of Ni-Cu-Ti in the near-spherical precipitates, respectively.

As depicted in Fig. 4(a), the heat-treated $Fe_{27}Ni_{27}Co_{26}Cu_{10}Ti_{10}$ HEA exhibits equiaxed grains similar to the as-cast sample, while the phase formed near the grain boundaries is different. A significant volume of needle-like phases is observed at the grain boundaries of the equiaxed grains, fully occupying these interfaces and exhibiting a tendency to extend into the grain interior. The high-magnification image [Fig. 4(b)] reveals that this needle-like phase does not appear along one particular direction, instead, it shows randomly distribution in different directions. The EDS result of Point 4 (listed in Table 1) reveals that the chemical composition of the grain interior after heat treatment does not change significantly and remains close to the nominal composition. However, Ni and Ti are more obviously enriched in the needle-like phase (Point 5) of the heat-treated HEA. The chemical composition of the needle-like phase is as follows: Fe: 13.22, Ni: 33.87, Co: 25.52, Cu: 7.49, Ti: 19.90 (at.%).

To further investigate the crystal structure, morphology, and elemental distribution of multiple phases in the as-cast $Fe_{27}Ni_{27}Co_{26}Cu_{10}Ti_{10}$ HEA, TEM analysis was conducted, as shown in Fig. 5. Figures 5(a–b) show the low-magnification bright-field (BF) TEM images of the region near the grain boundaries, illustrating that the needle-like phase grows along grain boundaries into intragranular and can cross two adjacent grains. Focusing on the region near the grain boundary, it is surprisingly found that some smaller bright white particles precipitated together with the near-spherical precipitates are

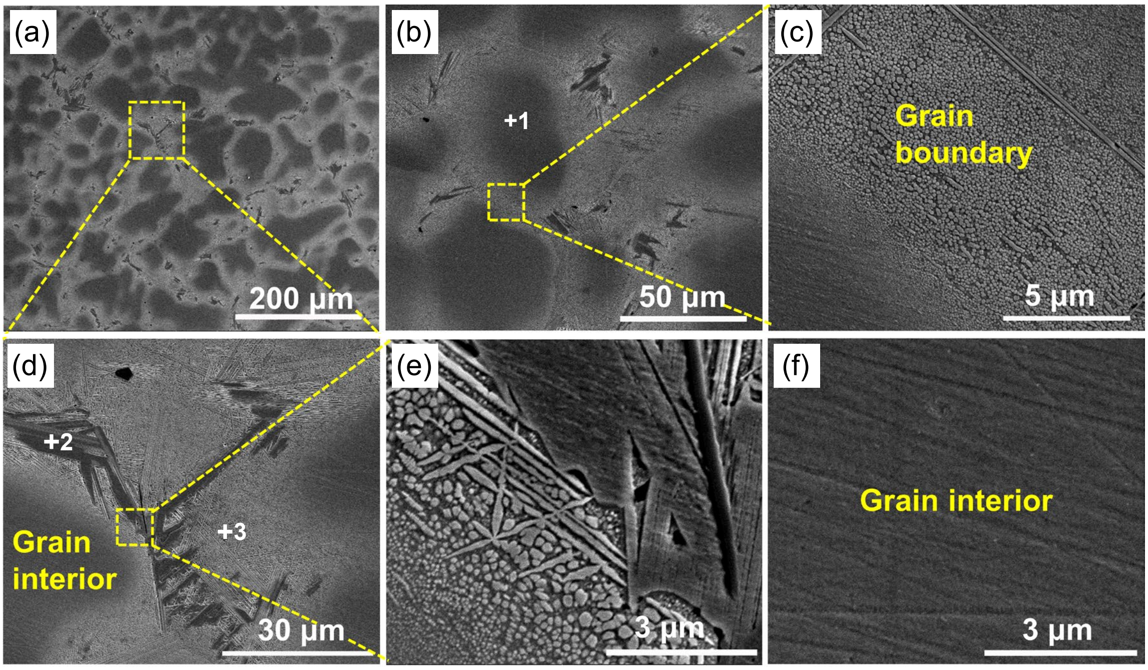

Fig. 3: SEM images of as-cast $Fe_{27}Ni_{27}Co_{26}Cu_{10}Ti_{10}$ HEA: (a) low-magnification image; (b) high-magnification image; (c) magnified image of the sample region marked in (b); (d) magnified image of square region in (a); (e) magnified image of square region in (d); (f) high-magnification SEM image of grain interior in (d)

Table 1: Chemical compositions (at.%) of as-cast and heat-treated $Fe_{27}Ni_{27}Co_{26}Cu_{10}Ti_{10}$ HEA samples analyzed by SEM-EDS with analyzed regions marked by different numbers in Figs. 3 and 4

State	Point	Fe	Ni	Co	Cu	Ti
Nominal composition	–	27	27	26	10	10
As-cast	1	30.80	26.16	26.42	8.87	7.75
	2	14.85	29.88	25.17	9.30	20.80
	3	21.74	28.43	24.97	10.66	14.20
Heat-treated	4	30.21	25.02	26.93	9.04	8.80
	5	13.22	33.87	25.52	7.49	19.90

observed in the TEM image, as shown in Fig. 5(c).

The weak super-lattice diffraction spots in the SAED pattern in the inset along the [011] zone axis demonstrate the ordered fcc structure. There are also high-density nano-sized spherical precipitates within the intragranular, as depicted in Fig. 5(d). The corresponding SAED pattern confirms the ordered $L1_2$ structure of these nanoprecipitates in the grain interior and their coherent relationship with the fcc matrix.

The specific crystal structure of the needle-like phase is further analyzed in Fig. 6. The location of the needle-like phase is identified in the BF-TEM image [Fig. 6(a)]. Then, the SAED pattern [Fig. 6(b)] corresponding to the selected area, indicated by the yellow circle in Fig. 6(a), can be obtained. By comparing the standard electron diffraction pattern, the positions of the lattice represented by the diffraction spots are calibrated, and the crystal structure of the needle-like phase is determined to be the

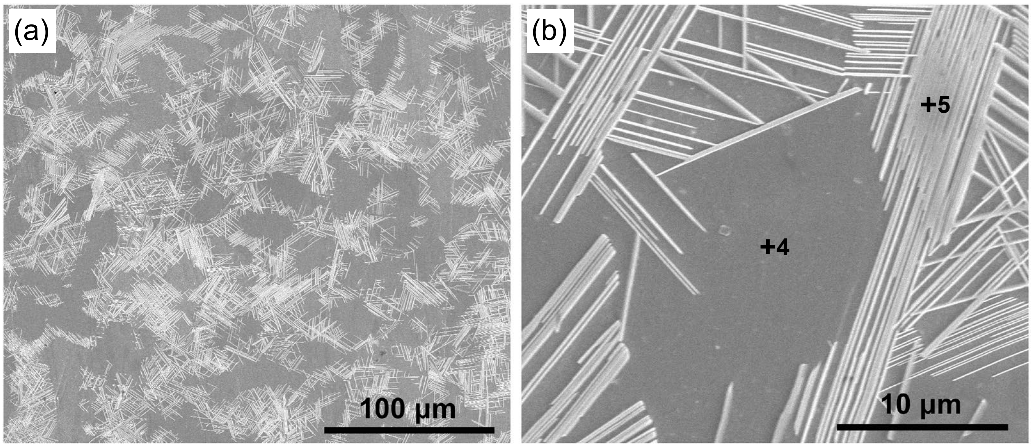

Fig. 4: SEM images of heat-treated $Fe_{27}Ni_{27}Co_{26}Cu_{10}Ti_{10}$ HEA: (a) low-magnification image; (b) high-magnification image

ordered D0$_{24}$-type η phase. Additionally, the small bright white particles can be noted to generate in abundance in the interstices of large near-spherical precipitates in Fig. 6(a).

Figure 7 shows the HR-TEM image of the as-cast $Fe_{27}Ni_{27}Co_{26}Cu_{10}Ti_{10}$ HEA, focusing on the grain interior. The interface between the precipitate and matrix, as shown in Fig. 7(a), confirming their fully coherent relationship. Figures 7(b) and (c) exhibit fast Fourier transform (FFT) patterns along the [011] zone axis corresponding to the matrix and precipitate, showing disordered fcc structure (A1) and ordered fcc structure (L1$_2$), respectively. HR-TEM image and FFT patterns provide further evidence of the "fcc+L1$_2$" structure in the grain interior.

The chemical compositions of the fcc matrix, precipitates, and η phase in the as-cast sample can be obtained by EDS/TEM analysis, and the results are summarized in Table 2. The fcc matrix is significantly enriched in Fe and slightly enriched in Co, while being depleted in Ni, Cu, Ti. In contrast, Ni and Ti exhibit a strong tendency to enrich in the precipitates, whereas the contents of Fe and Cu in the precipitates are pretty low. Interestingly, the η phase shares a similar chemical composition with the precipitates. It is also noteworthy that the content of Cu in these three phases is extremely low. Therefore, it is reasonable to assume that another bright white particle may have a very high degree of Cu enrichment.

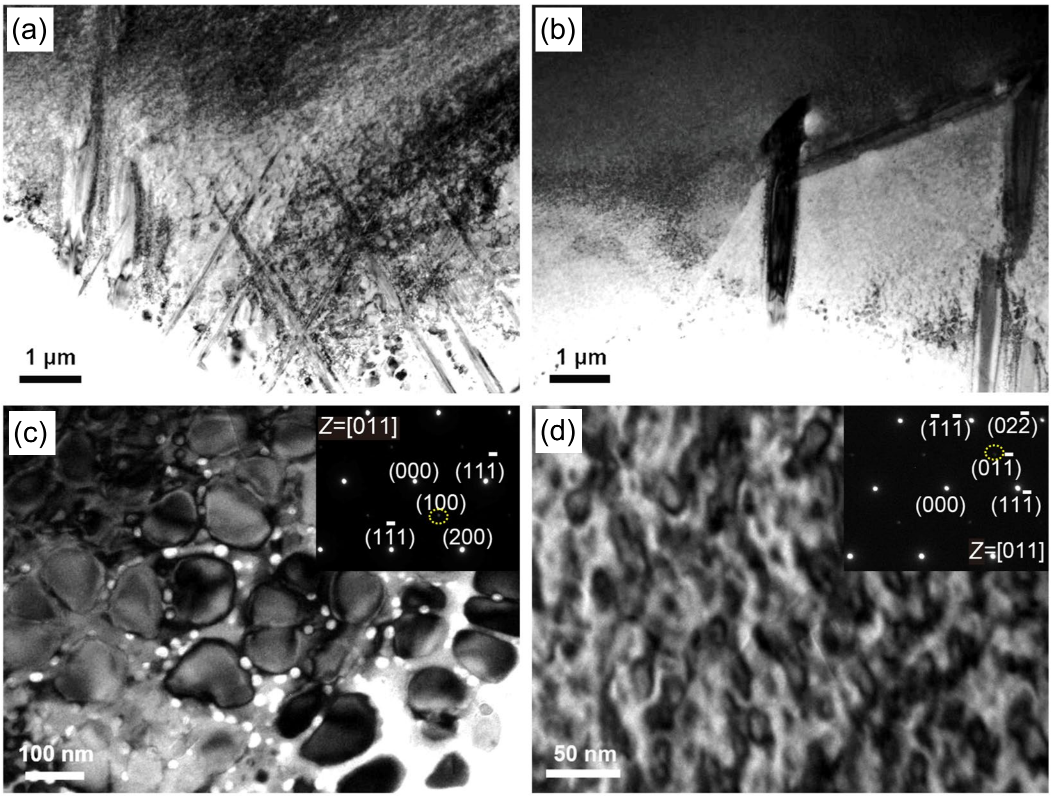

Fig. 5: Bright-field TEM images of as-cast $Fe_{27}Ni_{27}Co_{26}Cu_{10}Ti_{10}$ HEA: (a) and (b) low-magnification images; (c) and (d) high-magnification images closed to grain boundary (c) and grain interior (d) with corresponding SAED patterns

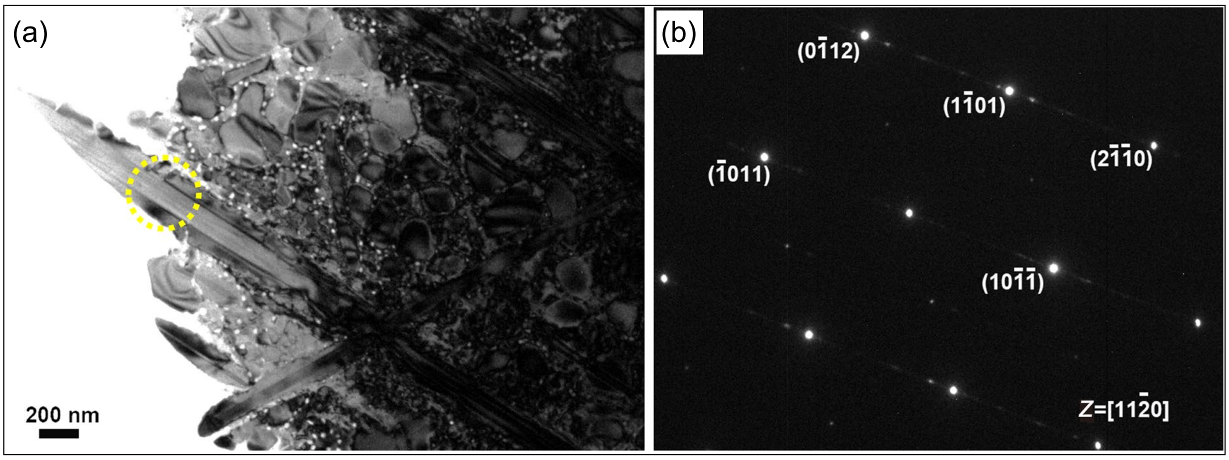

Fig. 6: Bright-field TEM image of needle-like η phase in as-cast $Fe_{27}Ni_{27}Co_{26}Cu_{10}Ti_{10}$ HEA (a) and SAED pattern corresponding to the needle-like η phase (b)

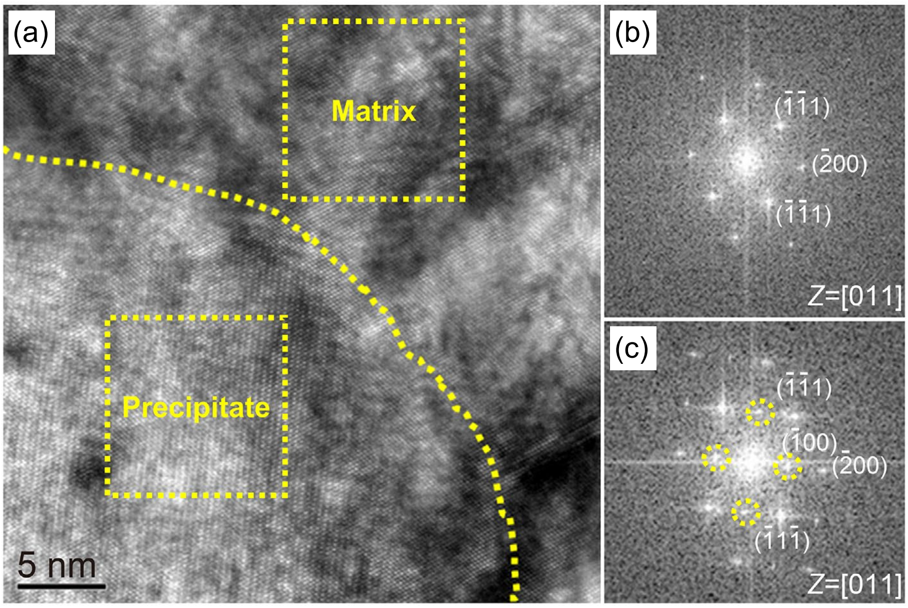

Fig. 7: HR-TEM of as-cast $Fe_{27}Ni_{27}Co_{26}Cu_{10}Ti_{10}$ HEA: (a) HR-TEM image of spherical precipitate and fcc matrix; (b) FFT of matrix, showing disordered fcc structure; (c) FFT of precipitate, showing ordered fcc structure ($L1_2$)

Table 2: Chemical compositions (in at.%) of as-cast and heat-treated $Fe_{27}Ni_{27}Co_{26}Cu_{10}Ti_{10}$ HEA samples analyzed by TEM-EDS and/or APT

State	Measure method	Phase	Fe	Ni	Co	Cu	Ti
As-cast	EDS/TEM	fcc matrix	41.95±2.45	19.33±2.33	29.54±1.35	5.52±0.82	3.66±0.42
	EDS/TEM	Precipitate	7.46±1.09	39.74±0.18	27.36±0.99	4.56±0.80	20.88±0.85
	EDS/TEM	η	8.62±1.35	37.68±3.00	27.22±2.79	5.61±0.66	20.78±0.79
	APT	fcc matrix	49.94±1.95	17.46±1.48	29.09±1.78	1.10±0.40	2.41±0.59
	APT	Precipitate	6.05±0.87	43.70±1.83	25.49±1.61	1.01±0.38	23.75±1.57
	APT	White particle	0.89±0.79	9.14±3.66	0.75±0.67	87.55±4.28	1.67±0.89
Heat-treated	EDS/TEM	fcc matrix	30.59±1.31	23.18±0.42	26.00±0.46	10.49±1.71	9.74±0.88
	EDS/TEM	η	8.09±0.50	37.72±0.45	23.85±0.35	5.54±0.18	24.80±0.43

3D APT reconstruction near the grain boundaries in the as-cast $Fe_{27}Ni_{27}Co_{26}Cu_{10}Ti_{10}$ HEA quantitatively illustrates the elemental partitioning of the constituent atoms, as depicted in Fig. 8. Figure 8(a) shows a 3D Ti-Cu map and two interfaces highlighted by 20at.% Ti and 50at.% Cu iso-concentration surface, respectively. The 20at.% Ti iso-concentration map delineates the outline of the large near-spherical precipitates near the grain boundaries, while the 50at.% Cu iso-concentration surface represents the outer contour of the small bright white particles. Two 1D concentration-depth profiles taken along the length direction of the cylinder "b" and "c" in (a) are displayed in Figs. 8(b) and (c), respectively. The chemical compositions of the fcc matrix, precipitates, and bright white particles in the as-cast sample are summarized in Table 2. It can be concluded that Ni (43.70at.%) and Ti (23.75at.%) are enriched in the large near-spherical precipitates, while the fcc matrix contains comparatively higher Fe (49.94at.%), as shown in Fig. 8(b). In contrast, the bright white particle exhibits an extremely high content of Cu (87.55at.%) and a slight Ni (9.14at.%), with almost no other constituent elements (Fe: 0.89at.%, Co: 0.75at.%, Ti: 1.67at.%). This elemental distribution confirms that the conjecture presented in the previous section is well-founded and consistent with the experimental observations.

The chemical compositions of the fcc matrix and precipitates obtained by the APT method are consistent with the EDS/TEM results. Combined with the SAED pattern in Fig. 5(c), it can be determined that the large near-spherical precipitates near the grain boundaries are ordered $L1_2$ precipitates. According to the previous research, the stoichiometry of the $L1_2$ precipitates could be regarded as $(Ni,Co)_3Ti$[12, 13]. The bright white particle contains almost 90at.% Cu, which can be approximately considered a pure Cu particle. The Cu atoms exhibit a disordered fcc structure, indicating that the Cu-rich bright particles are fcc-structured. The diffraction spots corresponding

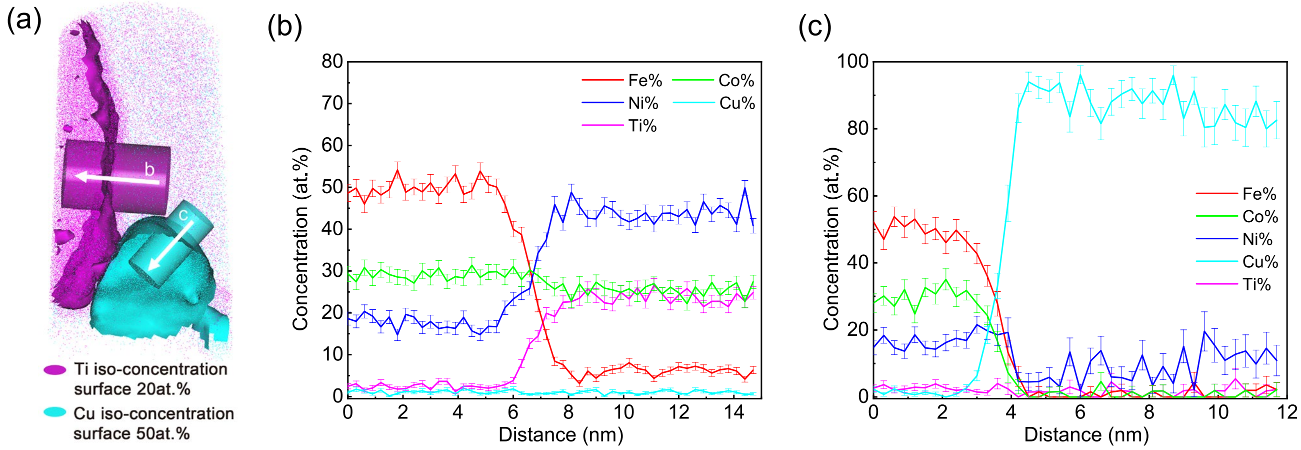

Fig. 8: APT analysis revealing elemental distributions across interfaces in as-cast $Fe_{27}Ni_{27}Co_{26}Cu_{10}Ti_{10}$ HEA: (a) 3D Ti-Cu map and two interfaces highlighted by 20at.% Ti and 50at.% Cu iso-concentration surfaces, respectively; (b) and (c) 1D compositional profiles taken along the length direction of the cylinder "b" and "c" in (a), respectively

to the Cu-rich particles are overlapped with the fcc matrix, resulting in the "fcc+$L1_2$" structure illustrated by the SAED pattern in Fig. 5(c). In summary, the as-cast $Fe_{27}Ni_{27}Co_{26}Cu_{10}Ti_{10}$ HEA consists of the fcc matrix with $L1_2$ nanoprecipitates in the intragranular, and needle-like η phase, large near-spherical $L1_2$ precipitates, and Cu-rich particles near the grain boundaries.

Figure 9 shows representative TEM images of the heat-treated $Fe_{27}Ni_{27}Co_{26}Cu_{10}Ti_{10}$ HEA near the grain boundaries. Some needle-like phases along various directions are embedded within the matrix, as shown in Fig. 9(a). The SAED pattern presented in Fig. 9(b) along the [011] zone axis corresponds to a disordered fcc structure without weak superlattice spots, suggesting no precipitates within the fcc matrix. A typical η-$D0_{24}$ structure is illustrated by the SAED pattern [Fig. 9(c)] along the $[11\bar{2}0]$ zone axis, indicating the crystal structure of the needle-like phase.

The elemental distribution of the heat-treated $Fe_{27}Ni_{27}Co_{26}Cu_{10}Ti_{10}$ HEA is characterized by high-angle annular dark-field scanning transmission electron microscopy (HAADF-STEM) image and its corresponding EDS elemental mapping (Fig. 10). It can be observed that Ni and Ti have a strong tendency to enrich in η phase, while all constituent elements exhibit homogenous distribution in the fcc matrix. Therefore, the absence of elemental segregation in the fcc matrix confirms that no precipitate is formed. Furthermore, the EDS/TEM results (Table 2) reveal a η-type phase with a detailed composition of 8.09at.% (Fe), 37.72at.% (Ni), 23.85at.% (Co), 5.54at.% (Cu), 24.80at.% (Ti), which is consistent with the chemical composition of the η phase in the as-cast HEA. Based on previously reported studies, the needle-like η phase presented in both the as-cast and heat-treated HEAs can be classified as a Ni_3Ti-type intermetallic with the $D0_{24}$ structure[26]. In conclusion, the heat-treated $Fe_{27}Ni_{27}Co_{26}Cu_{10}Ti_{10}$ HEA is composed of a fcc matrix with an amount of η phase.

Figure 11 shows the HR-TEM image and FFT patterns of the needle-like phase and matrix. Figure 11(a) demonstrates that the interfacial relationship between the elongated side of needle-like phase and matrix is fully coherent. Figures 11(b)

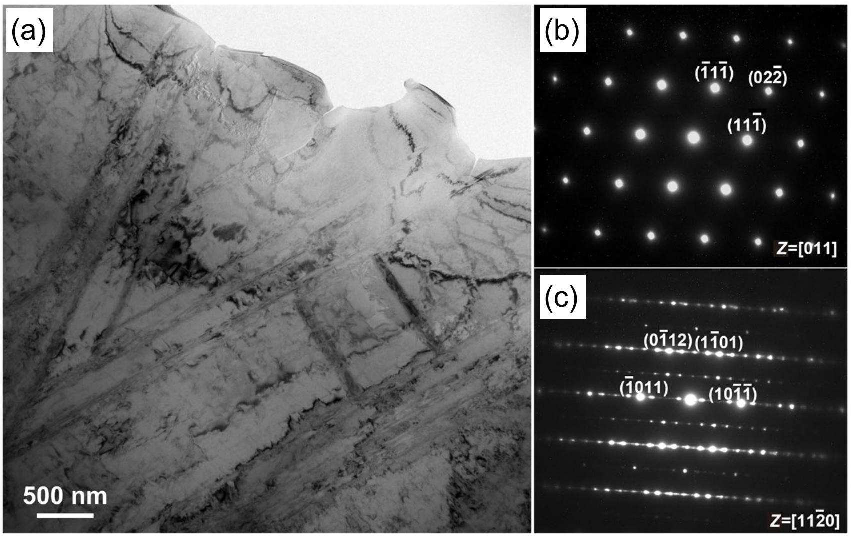

Fig. 9: TEM image of heat-treated $Fe_{27}Ni_{27}Co_{26}Cu_{10}Ti_{10}$ HEA: (a) bright-field TEM image; (b) SAED pattern of fcc matrix; (c) SAED pattern of needle-like η phase

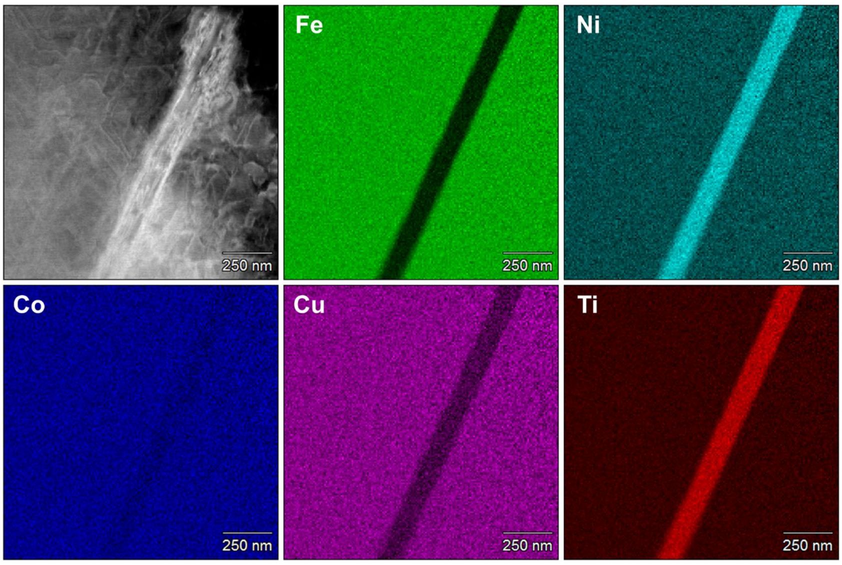

Fig. 10: HADDF-STEM EDS mapping of heat-treated $Fe_{27}Ni_{27}Co_{26}Cu_{10}Ti_{10}$ HEA, showing that component elements are uniformly distributed in fcc matrix, whereas needle-like η phase is Ni-Ti rich

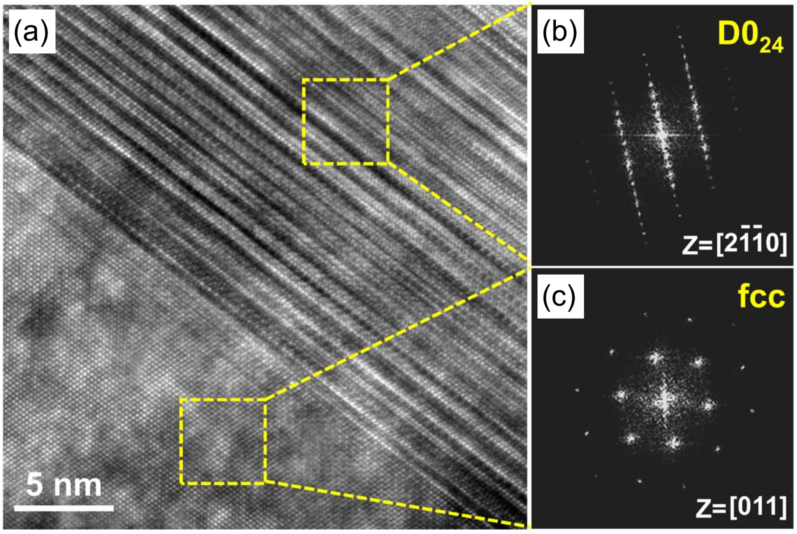

Fig. 11: HR-TEM of needle-like phase in heat-treated $Fe_{27}Ni_{27}Co_{26}Cu_{10}Ti_{10}$ HEA: (a) HR-TEM image of needle-like phase and matrix; (b) FFT patten of needle-like phase, showing η-$D0_{24}$ structure; (c) FFT pattern of matrix, showing fcc structure

and (c) show the FFT patterns corresponding to needle-like η phase and fcc matrix, respectively. HR-TEM results further validate that the heat-treated alloy displays a structure composed of fcc and η phases, without any additional phase.

The EDS/TEM and APT results indicate that the chemical compositions of the $L1_2$ precipitates and needle-like η phase are highly consistent, both of which display a noticeable tendency to enrich Ni, Co, and Ti (Table 2). This elemental enrichment tendency can be explained by the difference in mixing enthalpy between the constituent elements. The more negative mixing enthalpy of Ni-Ti (–35 kJ·mol^{-1}) and Co-Ti (–28 kJ·mol^{-1}) atom pairs promote the formation of the $(Ni,Co)_3Ti$-type phase with ordered structure such as $L1_2$ and $D0_{24}$[27].

The existence of the Cu-rich particles precipitated near the grain boundaries in the as-cast HEA could be due to the positive mixing enthalpy between Cu and other components, for example, Cu-Fe: 13 kJ·mol^{-1}, Cu-Co: 6 kJ·mol^{-1}, and Cu-Ni: 4 kJ·mol^{-1}. Although the Cu-Ti atom pair has a negative mixing enthalpy, its value (–9 kJ·mol^{-1}) is still apparently higher than the Ni-Ti and Co-Ti atom pairs, thus, Ti preferentially assists the nucleation of the $L1_2$ precipitates[26, 28]. The large, near-spherical $L1_2$ precipitates formed in the vicinity of grain boundaries consume nearly all available Ti, leading to the depletion of Ti in the surrounding matrix and the subsequent formation of small, bright white particles enriched in Cu, which appear as nearly pure Cu regions between the $L1_2$ precipitates. These Cu-rich particles then act as heterogeneous nucleation sites to accelerate the formation of $L1_2$ precipitates, culminating in a dense co-precipitation structure[29].

The distorted atomic arrangement at the interface gives grain boundaries higher energy than the transgranular, and this high-energy state encourages the grain boundaries to lower the nucleation energy barrier of the precipitates by providing additional driving force[30]. Additionally, solute atoms at the grain boundaries have enhanced diffusivity due to interface reaction, promoting their aggregation into clusters or new phases[31, 32]. Grain boundaries are the interfaces between grains with different orientations in polycrystalline materials. They can also be regarded as crystal defects and often serve as heterogeneous nucleation sites[33]. Therefore, multiple phases, including $L1_2$ precipitates, Cu-rich particles, and needle-like η phase, are generated near the grain boundaries of the as-cast $Fe_{27}Ni_{27}Co_{26}Cu_{10}Ti_{10}$ HEA.

Based on the above microstructure analysis, it can be concluded that a significant phase transformation occurs in $Fe_{27}Ni_{27}Co_{26}Cu_{10}Ti_{10}$ HEA after heat treatment at 1,000 °C for 4 h. Specifically, the microstructural evolution can be summarized as fcc+$L1_2$+Cu-rich+η phases to fcc+η phases. The $L1_2$ precipitates and Cu-rich particles may dissolve into the fcc matrix or transform into η phase during the high-temperature heat treatment. The specific reasons for the disappearance of the $L1_2$ precipitates and Cu-rich particles in heat-treated HEA are discussed below.

The $L1_2$ and η-$D0_{24}$ structures are related by different stacking sequences of identical close-packed ordered planes[34, 35]. The η-$D0_{24}$ phase exhibits an atomic arrangement of ABACABAC along the $[0001]_\eta$ direction, whereas the orders of the close-packed plane of the $L1_2$ phase follow the ABCABC law along the $[111]_{L1_2}$ direction. The atomic plane with an interface orientation relation of $(0001)_\eta//(111)_{L1_2}$ provides the necessary condition for the transformation of the $L1_2$ and η-$D0_{24}$ structures[24]. Another essential condition for the crystal structure transition from $L1_2$ to η-$D0_{24}$ is the extrinsic stacking faults (ESFs) caused by the climb of Frank dislocation partials[34]. Even if the above necessary conditions are fulfilled, sufficient driving force is still required to realize the $L1_2$ to η-$D0_{24}$ phase transition. As is well known, the lattice misfit between the η phase and fcc matrix is significantly larger than fcc and $L1_2$ with complete coherency, resulting in larger strain energy of the η phase. Additionally, the thermodynamic driving force offered by the high-temperature heat treatment facilitates the phase transformation.

The η-$D0_{24}$ phase forms at the expense of the $L1_2$ phase, and shares the same chemical composition, $(Ni, Co)_3Ti$, as that of the $L1_2$ phase. This leads to a deficiency of the constituent elements necessary for the nucleation of $L1_2$ phase and lowers the degree of supersaturation in the fcc matrix, making it more difficult for the formation of $L1_2$ phase. Furthermore, the abundant needle-like η phase precipitated at the grain boundaries plays a key role in adsorbing and storing the impurities and defects, which decreases the interfacial energy and defect density in the grain boundary region[25, 36]. As a consequence, both the reduction in heterogeneous nucleation sites and the driving force increase the difficulty of nucleation. Therefore, when the η-$D0_{24}$ phase fully occupies the grain boundaries, the formation of other phases ($L1_2$ precipitates and Cu-rich particles) is strongly suppressed. Moreover, the η-$D0_{24}$ phase can effectively pin the grain boundaries, thus inhibiting grain boundary migration from the kinetics perspective. This decrease in the grain boundary migration rate also suppresses the nucleation of the precipitates near the grain boundaries[37].

3.2 Mechanical properties

Figure 12 displays the tensile engineering stress-strain curves of the as-cast and heat-treated $Fe_{27}Ni_{27}Co_{26}Cu_{10}Ti_{10}$ HEA at room temperature. The specific values of the mechanical properties, including the yield strength ($\sigma_{0.2}$), ultimate tensile strength (σ_{UTS}), and total elongation, are summarized in Table 3. The as-cast HEA exhibits a notable strength-ductility trade-off, with a superior yield strength of 1,020 MPa, yet a poor total elongation of 0.9%. Compared to the as-cast HEA, the heat-treated HEA demonstrates significantly improved ductility, with a total elongation increasing to 7.5%. Meanwhile, the sacrifice in the strength of the heat-treated HEA remains within acceptable limits, the yield strength and ultimate tensile strength are 662 MPa and 925 MPa, respectively.

To further investigate the mechanical behavior during tensile deformation, the fracture morphology of both the as-cast and heat-treated samples after tensile tests is illustrated in Fig. 13. As displayed in Fig. 13(a), a large cleavage facet can be observed in the as-cast sample. Figure 13(b) presents the fracture morphology in the region near grain boundaries, where thin, elongated cleavage facets in multiple directions coincide with the needle-like η phase (indicated by the yellow dash line). This observation demonstrates that the cracks propagate along the η phase during tensile deformation. The dense shallow dimples shown in Fig. 13(c) are associated with the dispersive distribution of the $L1_2$ precipitate within the grains of the as-cast sample. Studies have indicated that when the size of dimples is comparable to the spacing of

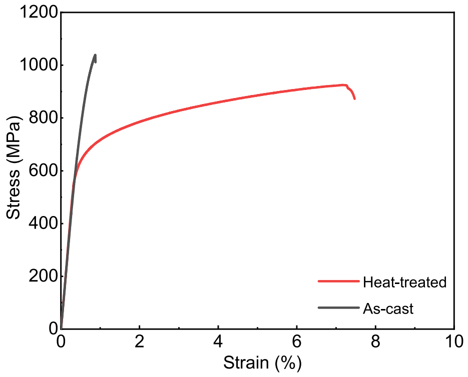

Fig. 12: Representative tensile engineering stress-strain curves of as-cast and heat-treated $Fe_{27}Ni_{27}Co_{26}Cu_{10}Ti_{10}$ HEA samples at room temperature

Table 3: Yield strength ($\sigma_{0.2}$), ultimate tensile strength (σ_{UTS}) and total elongation of as-cast and heat-treated $Fe_{27}Ni_{27}Co_{26}Cu_{10}Ti_{10}$ HEA samples

Alloys	$\sigma_{0.2}$ (MPa)	σ_{UTS} (MPa)	Total elongation (%)
As-cast	1,020±10.6	1,040±11.2	0.9±0.2
Heat-treated	662±6.5	925±8.8	7.5±0.5

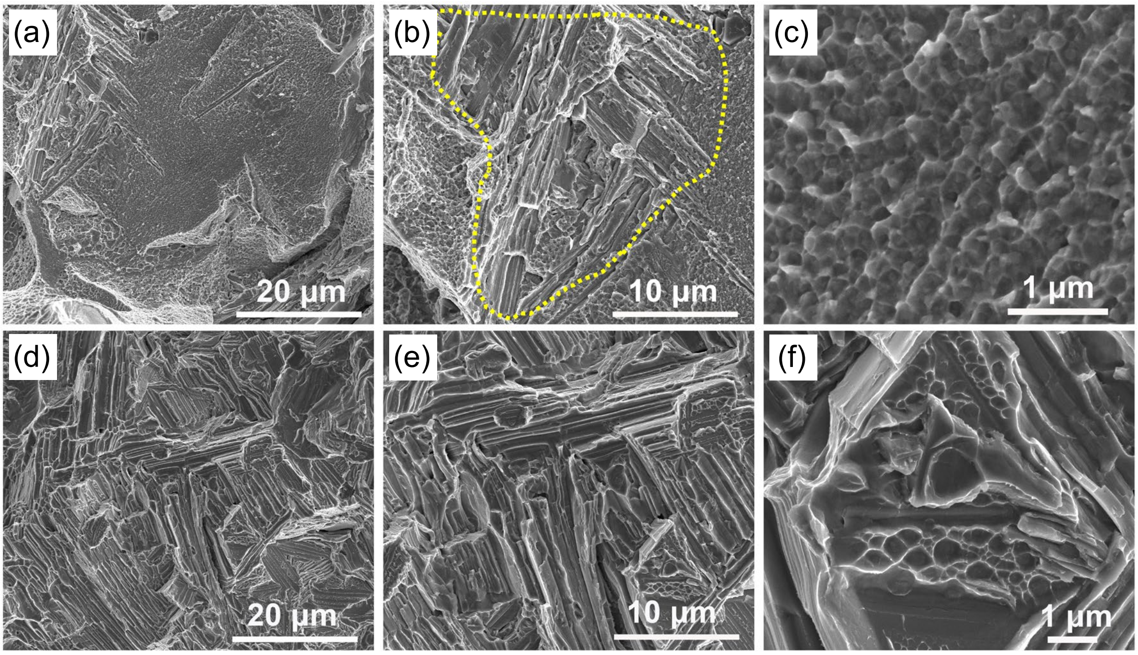

Fig. 13: Fracture morphologies of HEA samples after tension tests: (a), (b) and (c) as-cast; (d), (e) and (f) heat-treated

the inclusions, the η phase may promote the formation of microvoids. Consequently, cracks tend to propagate through the weak interfaces with relatively low cohesion forces[18]. As a result, the as-cast samples experience premature brittle fracture during the tensile process.

As manifested in Figs. 13(d–e), different from the as-cast sample, the fracture morphology of the heat-treated sample exhibits significantly denser, more multidirectional, and elongated cleavage facets. These cleavage facets, which exhibit shapes complementary to the needle-like η phase, intersect with each other and completely cover the entire fracture surface. In the enlarged SEM image [Fig. 13(f)], a small amount of dimples can be observed in the gap between the thin and long cleavage facets. The high-density needle-like η phase in different directions can intercept each other, effectively preventing the expansion of plastic deformation-induced cracks.

The heterogeneous co-precipitation structure near the grain boundaries in the as-cast HEA is detrimental to the ductility, which is the primary cause of premature brittle fracture. After high-temperature heat treatment, the co-precipitation structure near grain boundaries transforms into a dense, interconnected network of needle-like η phases that are intricately interspersed. The η phase exhibits an ordered Ni_3Ti-type hcp structure, and has a specific orientation relationship with the disordered fcc phase, that is, $\{11\bar{1}1\}_{fcc}//\{0001\}_{\eta}$ and $[011]_{fcc}//[11\bar{2}0]_{\eta}$[38]. The interfacial relationship between the η phase and fcc phase can be classified into two types: the non-coherent interface corresponding to the tip of the η phase, and the coherent interface associated with the macroscopically elongated side[27]. The tip of the η phase, which features a non-coherent interface, acts as the growth front of the phase due to its higher interfacial energy. As a result, the phase grows preferentially along the macroscopically elongated direction, and this interfacial characteristic contributes to the needle-like morphology of the η phase.

The needle-like η phase greatly influences the mechanical properties of the heat-treated HEA. At the macro level, the needle-like η phase can deflect cracks during propagation, leading to the formation of more zigzag and jagged cracks. This deflection process consumes more energy, making it harder for cracks to continue propagating[39, 40]. From the micro perspective, the η/fcc interface with a certain degree of lattice mismatch enables the η phase to serve as the dislocation source to generate new dislocations as strain increases[41]. Meanwhile, the needle-like η phase contributes to pinning the interface and impede the movement of dislocations. Compared to classical equiaxed or near-equiaxed precipitates, such as spherical, cubic, and rod-shaped particles, needle-like precipitates exhibit anisotropic interactions with dislocation motion due to their high length-diameter ratio and preferential alignment along specific crystallographic directions. When dislocations glide perpendicular to the long axis of needle-like precipitates, the effective hindrance length increases, forcing dislocations to undergo extensive bending or looping. If dislocations move parallel to the long axis, they accumulate densely owing to the continuous distribution of needle-like precipitates[36]. In contrast, classical precipitates exhibit random spatial distributions and interact with dislocations in an isotropic, point-like manner, featuring shorter bypass paths and smaller hindrance ranges. The macroscopic effect on cracks and microscopic effect on dislocations of the needle-like η phase synergistically affect the mechanical behavior of the heat-treated HEA.

As discussed above, the needle-like η phase can strongly hinder the crack propagation and dislocation movement, contributing to the improvement of the ductility. Furthermore, the fcc matrix also exerts a substantial influence on improving the ductility of the heat-treated alloy. Unlike the fcc+$L1_2$

structure in the grain interior of the as-cast HEA, the heat-treated HEA exhibits a single-phase fcc-structured matrix without any precipitates. The ordered $L1_2$ nanoprecipitates exhibit higher hardness and strength than the fcc matrix; thus, the single-phase fcc matrix exhibits superior ductility to the fcc matrix containing $L1_2$ precipitates. The softer single-phase fcc structure possesses greater dislocation storage capacity and load bearing capacity, which is also conducive to enhancing the ductility of the alloy[42]. In summary, the phase transformation from fcc+$L1_2$+Cu-rich+η phases in the as-cast HEA to fcc+η phases in the heat-treated HEA significantly improves the comprehensive mechanical properties of the materials, highlighting the strengthening effect of the sole η phase in fcc-structured HEAs.

4 Conclusions

In this work, the as-cast and heat-treated $Fe_{27}Ni_{27}Co_{26}Cu_{10}Ti_{10}$ HEA samples were successfully designed and fabricated. The microstructural evolution, phase transformation, and mechanical behavior were systematically investigated. Based on the studies carried out, the main findings are as follows:

(1) The microstructural evolution could be summarized as fcc+$L1_2$+Cu-rich+η phases in the as-cast HEA to fcc+η phases in the heat-treated HEA. The formation of the $L1_2$ and Cu-rich phases is significantly suppressed during high-temperature heat treatment. The phase transition between the $L1_2$ and η-$D0_{24}$ phases is also analyzed in detail.

(2) The mechanical properties of the heat-treated HEA are significantly improved compared to the as-cast HEA, and the total elongation increases from 0.9% to 7.5%. At the same time, the yield strength and ultimate tensile strength remain at 662 MPa and 925 MPa, respectively. The needle-like η phase affects the mechanical behavior by impeding crack expansion and dislocation movement. Additionally, the soft single-phase fcc-structured matrix also contributes to the increase in ductility.

This work sheds light on understanding the strengthening mechanisms of the sole η-$D0_{24}$ phase in the fcc-structured HEAs, providing a new approach for enhancing mechanical properties and broadening the research potential of precipitate-strengthened alloys.

Acknowledgments

Authors wish to acknowledge the National Key Research and Development Program of China (Grant No. 2024YFB4608600), the International Science and Technology Cooperation Project of Guangdong Province (Grant No. 2023A0505050154), the Basic and Applied Basic Research Foundation of Guangdong Province (Grant No. 2023A1515012363), the National Natural Science Foundation of China (Grant No. 52103360), the Pearl River Talent Program (Grant No. 2021QN02C766), and the technical support of Sinoma Institute of Materials Research (Guang Zhou) Co., Ltd.

Conflict of interest

The authors declare that they have no known competing financial interests or personal relationships that could have appeared to influence the work reported in this paper.

References

[1] Mu Y, He L, Deng S, et al. A high-entropy alloy with dislocation-precipitate skeleton for ultrastrength and ductility. Acta Materialia, 2022, 232: 117975.
[2] Pan Q, Zhang L, Feng R, et al. Gradient cell-structured high-entropy alloy with exceptional strength and ductility. Science, 2021, 374(6570): 984–989.
[3] Liu S, Duan J, Zhang M, et al. Correlation of microstructure, mechanical properties and corrosion behavior in a Ni34Co28Cr28Al10 multi-principal element alloy with outstanding corrosion resistance. Corrosion Science, 2024, 228(1): 111835.
[4] Moravcik I, Hornik V, Minárik P, et al. Interstitial doping enhances the strength-ductility synergy in a CoCrNi medium entropy alloy. Materials Science and Engineering: A, 2020, 781(3): 139242.
[5] Ding L, Hilhorst A, Idrissi H, et al. Potential TRIP/TWIP coupled effects in equiatomic CrCoNi medium-entropy alloy. Acta Materialia, 2022, 234: 118049.
[6] Gludovatz B, Hohenwarter A, Thurston K V S, et al. Exceptional damage-tolerance of a medium-entropy alloy CrCoNi at cryogenic temperatures. Nature Communications, 2016, 7: 10602.
[7] Otto F, Dlouhý A, Somsen C, et al. The influences of temperature and microstructure on the tensile properties of a CoCrFeMnNi high-entropy alloy. Acta Materialia, 2013, 61(15): 5743–5755.
[8] Liu L Y, Zhang Y, Han J H, et al. Nanoprecipitate-strengthened high-entropy alloys. Advanced Science, 2021, 8(23): 2100870.
[9] Gangireddy S, Gwalani B, Mishra R S. Grain size dependence of strain rate sensitivity in a single phase FCC high entropy alloy $Al_{0.3}CoCrFeNi$. Materials Science and Engineering: A, 2018, 736(8): 344–348.
[10] Coury F G, Wilson P, Clarke K D, et al. High-throughput solid solution strengthening characterization in high entropy alloys. Acta Materialia, 2019, 167: 1–11.
[11] Chu C, Chen W, Huang L, et al. Exceptional strength-ductility synergy at room and liquid nitrogen temperatures of $Al_{7.5}Co_{20.5}Fe_{24}Ni_{24}Cr_{24}$ high-entropy alloy with hierarchical precipitate heterogeneous structure. International Journal of Plasticity, 2024, 175(11): 103939.
[12] He J Y, Wang H, Huang H L, et al. A precipitation-hardened high-entropy alloy with outstanding tensile properties. Acta Materialia, 2016, 102: 187–196.
[13] Zhao Y L, Yang T, Tong Y, et al. Heterogeneous precipitation behavior and stacking-fault-mediated deformation in a CoCrNi-based medium-entropy alloy. Acta Materialia, 2017, 138: 72–82.
[14] Yang T, Zhao Y L, Fan L, et al. Control of nanoscale precipitation and elimination of intermediate-temperature embrittlement in multicomponent high-entropy alloys. Acta Materialia, 2020: 47–59.
[15] Yen S Y, Liu Y C, Chu S H, et al. B2-strengthened Al-Co-Cr-Fe-Ni high entropy alloy with high ductility. Materials Letters, 2022, 325(6): 132828.
[16] Jo Y H, Choi W M, Sohn S S, et al. Role of brittle sigma phase in cryogenic-temperature-strength improvement of non-equi-atomic Fe-rich VCrMnFeCoNi high entropy alloys. Materials Science and Engineering: A, 2018, 724(3): 403–410.

[17] Lin K, Chen S C, Lin H C, et al. Enhancement in mechanical properties through an FCC-to-HCP phase transformation in an Fe-17.5Mn-10Co-12.5Cr-5Ni-5Si (in at.%) medium-entropy alloy. Journal of Alloys and Compounds, 2022, 898: 162765.

[18] Shen P K, Liu H C, Huang C Y, et al. Microstructure and mechanical properties of medium-entropy alloys with a high-density η-$D0_{24}$ phase. Materials Characterization, 2022, 185(101): 111713.

[19] Fan L, Yang T, Zhao Y, et al. Ultrahigh strength and ductility in newly developed materials with coherent nanolamellar architectures. Nature Communications, 2020, 11: 240.

[20] Chou T H, Li W P, Chang H W, et al. Suppressing temperature-dependent embrittlement in high-strength medium-entropy alloy via hetero-grain/precipitation engineering. Scripta Materialia, 2023, 229: 115577.

[21] Zhao Y L, Yang T, Zhu J H, et al. Development of high-strength Co-free high-entropy alloys hardened by nanosized precipitates. Scripta Materialia, 2018, 148: 51–55.

[22] Hou Y D, Li X N, Li Z M, et al. Achieving optimal comprehensive properties in heat resistant Cu-based alloys by regulating complex elemental interaction. Materials Characterization, 2024, 216: 114308.

[23] Yuan J L, Wu Y C, Liaw P K, et al. Remarkable cryogenic strengthening and toughening in nano-coherent CoCrFeNiTi$_{0.2}$ high-entropy alloys via energetically-tuning polymorphous precipitates. Acta Materialia, 2021, 842: 143111. http://doi.org/10.2139/ssrn.3949513.

[24] Chu C, Chen W, Fu Z, et al. Realizing good combinations of strength-ductility and corrosion resistance in a Co-free $Fe_4Ni_4Mn_2CrTi$ high-entropy alloy via tailoring Ni/Ti-rich precipitates and heterogeneous structure. Materials Science and Engineering: A, 2023, 878(3): 145223.

[25] Ou M, Ma Y, Ge H, et al. Microstructure evolution and mechanical properties of a new cast Ni-base superalloy with various Ti contents. Journal of Alloys and Compounds, 2018, 735: 193–201.

[26] Chu C, Hao L, Chen W, et al. Phase transformations and mechanical behavior in a non-equiatomic $Ti_{10}Fe_{30}Co_{30}Ni_{30}$ medium-entropy alloy. Materials Science and Engineering: A, 2022, 832(12): 142429.

[27] Zhang B, Mu W, Cai Y. The effect of cooling rate on the precipitation behavior and fracture toughness of the η phase in LDED CoCrFeNiTi high-entropy alloy. Materials Science and Engineering: A, 2024, 914(8): 147172.

[28] Sharma A, Lee H, Ahn B. Tailoring compressive strength and absorption energy of lightweight multi-phase AlCuSiFeX (X=Cr, Mn, Zn, Sn) high-entropy alloys processed via powder metallurgy. Materials, 2021, 14(17): 4945. http://doi.org/10.3390/MA14174945.

[29] Gwalani B, Gorsse S, Soni V, et al. Role of copper on L1$_2$ precipitation strengthened fcc based high entropy alloy. Materialia, 2019, 6(1): 100282.

[30] Kokkula P C, Samanta S, Mandal S, et al. Kinetics of pearlite transformation: The effect of grain boundary engineering. Acta Materialia, 2025, 284(7): 120641.

[31] Jägle E A, Mittemeijer E J. The kinetics of grain-boundary nucleated phase transformations: Simulations and modelling. Acta Materialia, 2011, 59(14): 5775–5786.

[32] Wang Z, Xiao H, Chen W, et al. Effect of grain boundary and reinforced particles on grain boundary precipitates in TiB$_2$/Al-Zn-Mg-Cu composite. Materials Characterization, 2023, 197(12): 112703.

[33] Yao Y C, Euesden R, Curd M E, et al. Effect of cooling rate on the composition and chemical heterogeneity of quench-induced grain boundary η-phase precipitates in 7xxx aluminium alloys. Acta Materialia, 2024, 262: 119443. http://doi.org/10.1016/j.actamat.2023.119443.

[34] Kear B H, Giamei A F, Silcock J M, et al. Slip and climb processes in γ′ precipitation hardened nickel-base alloys. Scripta Metallurgica, 1968, 2(5): 287–293.

[35] Hagihara K, Nakano T, Umakoshi Y. Plastic deformation behaviour in Ni_3Ti single crystals with $D0_{24}$ structure. Acta Materialia, 2003, 51(9): 2623–2637.

[36] Ma S, Wang M, Ju Y, et al. Atomic-scale observation of the interfaces between η and γ matrix in ATI718Plus. Materials Characterization, 2024, 215(7): 114196.

[37] Ouyang H, Li Y, Guo C, et al. Differential effects of Fe, Ti and Fe+Ti addition on the discontinuous precipitation and properties of Cu-Ni-Sn alloys. Materials Characterization, 2024, 212(1). http://doi.org/10.1016/j.matchar.2024.114007.

[38] Suk J I, Hong S H, Nam S W. Crystallographic orientation relationships among η-Ni_3Ti precipitate, reverted austenite, and martensitic matrix in Fe-10Cr-10Ni-2W maraging alloy. Metallurgical Transactions: A, 1993, 24(12): 2643–2652.

[39] Williams W M, Shabani M, Jablonski P D, et al. Fatigue crack growth behavior of the quaternary 3d transition metal high entropy alloy CoCrFeNi. International Journal of Fatigue, 2021, 148(12): 106232.

[40] Pineau A. Crossing grain boundaries in metals by slip bands, cleavage and fatigue cracks. Philosophical Transactions of the Royal Society: A: 2015, 373(2038): 20140131. http://doi.org/10.1098/rsta.2014.0131.

[41] Zhai T, Jiang X P, Li J X, et al. The grain boundary geometry for optimum resistance to growth of short fatigue cracks in high strength Al-alloys. International Journal of Fatigue, 2005, 27(10–12): 1202–1209.

[42] Jiang K, Zhang Q, Li J, et al. Abnormal hardening and amorphization in an FCC high entropy alloy under extreme uniaxial tension. International Journal of Plasticity, 2022, 159(8): 103463.